Low Temperature Raman Imaging of Component Distribution in Micron-Size Droplets

Qishen Huang[1, 2], *Peter J. Vikesland*[1, 2]

[1]Department of Civil and Environmental Engineering, Virginia Tech, Blacksburg, Virginia 24061, United States

[2]Virginia Tech Institute of Critical Technology and Applied Science (ICTAS) Sustainable Nanotechnology Center (VTSuN), Blacksburg, Virginia 24061, United States

Keywords: Raman imaging, ice nucleation, ammonium sulfate, micron-size droplets, Surface-enhanced Raman spectroscopy (SERS), cloud formation, atmospheric droplets.

TOC Graphic

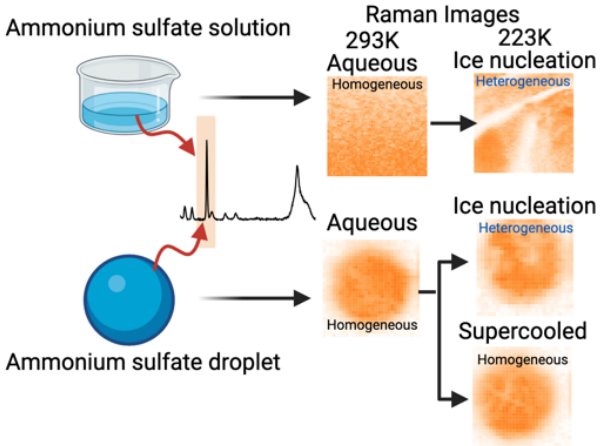

Abstract

Atmospheric droplets exhibit heterogeneity due to their distinct mixing states and phases. Ice nucleation is a common and stochastic atmospheric process that potentially enhances differences between individual droplets. In this study, we investigated the distribution of chemical moieties within micron-size droplets by recording spatial maps of sulfate, ice crystals, and gold nanoparticles (AuNPs) via Raman imaging at 293K and 223K. We observed a spatially even distribution of sulfate in ammonium sulfate (AS) solutions and droplets at 293K, as well as in supercooled AS droplets at 223K. Spatially enriched sulfate, expelled from ice crystals, appeared in frozen droplets and bulk solution at 223K. Interestingly, a fraction of the frozen droplets exhibited spatially enriched sulfate distributions, while others froze evenly. A higher percentage of more evenly distributed droplets were found for higher initial AS concentrations. We differentiated the droplets as supercooled or frozen according to the brightness of the collected optical images. Using Raman images of the AS droplets, we determined that >93% of the supercooled droplets were evenly distributed, while >90% of the frozen droplets were spatially enriched due to ice nucleation. We suggest that localized ice nucleation, within supercooled droplets, and glass formation, within completely frozen droplets are the major factors contributing to the remainder of the droplets (~10%). The different component distributions reflect the stochastic nature of ice nucleation. We also investigated the distribution of functionalized pH sensing AuNPs within frozen AS droplets and observed an independent distribution of AuNPs that differed from either the AS distribution or the ice nucleation sites. The relative peak intensity of the Raman spectrum of AuNPs changed at 223K compared to its room temperature spectrum, which suggests that the formation of ice crystals in the vicinity of AuNPs at 223K altered the spectral behavior of the functionalized nanoparticles.

Introduction

Particles and droplets dictate cloud radiative properties by scattering and absorbing solar and terrestrial radiation;[1] by serving as cloud condensation nuclei;[2,3] and through their involvement in atmospheric chemical processes.[4,5] Atmospheric ice particles, which can serve as cloud condensation nuclei and atmospheric reaction sites, form either through homogeneous nucleation of supercooled droplets or by heterogeneous nucleation from ice nuclei (e.g., immersion freezing, contact freezing, deposition nucleation).[1,6,7] Due to the relative rarity of airborne ice nuclei, supercooled droplets are atmospherically ubiquitous and are found from the surface layer to the upper troposphere.[8,9] Accordingly, homogeneous nucleation is important for the formation of mixed-phase clouds as it occurs in supercooled aqueous droplets when the ice saturation ($S_i = \frac{P_{H_2O}}{P_{ice}}$) is high (where $P_{\mathrm{H_2O}}$ is the equilibrium partial pressure of water at the freezing temperature and P_{ice} is the vapor pressure of ice at the freezing temperature).[10–13]

Individual aerosols and droplets can be subjected to different atmospheric processes and thus exhibit unique properties that reflect their prior histories. Atmospheric aerosols and droplets with the same composition can have differential properties depending on differences in mixing state.[14] The phases within individual aerosols and droplets may be solid or liquid, or may be a mixture of both as a result of their composition, the ambient conditions, and the stochastic nature of nucleation and crystallization.[15–19] Accordingly, even for consistent environmental conditions and droplet compositions, droplets can stabilize in various states and phases. For example, nucleation and crystallization can be hindered in some droplets thus resulting in formation of an amorphous solid or ‘glassy’ state instead of ice crystal formation.[20]

Ammonium sulfate (AS) particles and droplets are important constituents of upper tropospheric clouds.[21] Accordingly, understanding the supercooling and nucleation behavior of AS particles and droplets is important. Previous studies have investigated ice formation temperature and nucleation kinetics;[10,22] however, the exact distribution of AS in droplets upon freezing requires study since the AS internal distribution can affect droplet properties, such as pH, and in turn alter droplet-atmosphere interactions.[23,24]

Vibrational spectroscopies, such as infrared (IR)[21,25,26] and Raman,[27–29] have recently been shown to be useful tools for the investigation of ice nucleation and phase transitions in cloud droplets. Raman spectroscopy specifically, provides abundant chemical detail and higher spatial resolution compared to IR.[30] Using single-particle Raman spectroscopy, researchers have characterized mixing-states, phase transition, and ice nucleation of atmospherically relevant particles and aerosols.[31–35] The studies rely mainly on Raman spectral variations (e.g., peak location, peak intensity) which provide chemical information about the system. Raman images, compared to Raman spectra, contain additional information that reflect the spatial distribution of the collected spectra. Schill and Tolbert applied Raman line-mapping to investigate heterogeneous ice nucleation on simulated sea-spray aerosol.[36] Such line-maps can be further expanded to 2-D and 3-D Raman images to obtain detailed spatial distribution and chemical variation of the interested species. Functionalized gold nanoparticles (AuNPs) enabled surface enhanced Raman spectroscopy can provide steady and intense Raman signals with high enhancement factor; moreover, the spectra of functionalized AuNPs are responsive to chemical changes (e.g., pH) in their vicinity.[23,37,38] Particles in the atmosphere are important as they can serve as cloud condensation and ice nuclei, and recent studies have shown the formation of gold nanocrystals in supersaturated solutions.[7] Accordingly, the addition of AuNPs to micron-size droplets may provide

information with respect to the crystallization of droplet components. In this study, we explored the feasibility of using confocal Raman and surface-enhanced Raman spectroscopic (SERS) imaging to characterize the heterogeneity of individual micron-scale droplets, to probe droplet component distribution, and to examine the correlation between the distribution patterns of chemical constituents, ice crystals, and AuNPs in both supercooled and phase-transitioned droplets.

Experimental Methods

Droplet generation and collection. Micron-size droplets were generated from prepared solutions (0.1-3M ammonium sulfate (AS); 1M ammonium nitrate (AN); and 1M phosphate buffer (PB)) using a commercial atomizer (TSI 3076, TSI Inc.). Suspensions and droplets containing pre-synthesized pH nanoprobe - 4-mercaptobenzoic acid (4-MBA) functionalized AuNPs[37] - were studied separately. The atomizer was operated in a custom chamber at 95% RH.[38] Mixtures containing 2 mL of probe suspension and 3 mL of experimental solution were aerosolized and then collected for 2 minutes on a superhydrophobic filter fixed ≈ 0.5 cm away from the atomizer outlet. The superhydrophobic filter was prepared by coating 100 μL of AEROSIL-acetone suspension (4 g/L) onto a PVDF filter (Millipore Sigma) via air-drying. The contact angle of droplets collected on this substrate was ≈147° (Figure S1). The filter was transferred into a Linkam THM600 thermostage for temperature control and Raman imaging.

Freezing solution and droplets. The freezing of solutions and droplets was characterized using a Linkam THM600 thermostage. The accuracy of the temperature control of the thermostage was evaluated using a thermogun (Figure S2). The rate of temperature decrease provided by the thermostage can vary from 0.1 to 100K/min with 173K the lowest temperature possible. A temperature change rate of 10K/min was elected for this study.

Raman imaging and image processing. Raman imaging was conducted at both 293K (20°C, 95% RH) and 223K (-50°C) to observe both solutions and droplets. All frozen droplets were equilibrated at 223K for 20 min prior to Raman imaging, as the observed optical images showed negligible change with either longer freezing times or lower temperatures (down to 193K, Figure S3). Raman images were collected using a confocal Raman microscope (WITec Alpha 500R) and a 50× objective lens and a 633 nm laser. The laser spot has a lateral size of 0.68 μm, a vertical size of 3.2 μm, and an excitation volume of 1.5 μm^3. The spatial resolution of each Raman image was 1 μm^2/pixel with each pixel containing the averaged Raman signal from the excitation volume. The laser was initially focused at the droplet centroid and the integration time was 1 s for all measurements. All Raman images were denoised and smoothed using a Gaussian filter. This image processing method was selected out of three common methods (median filter, Gaussian filter, and fast and flexible denoising convolutional neural network) based upon having the lowest mean square error (MSE) and highest peak signal-to-noise-ratio (PSNR) (Figure S4).

Results and Discussion

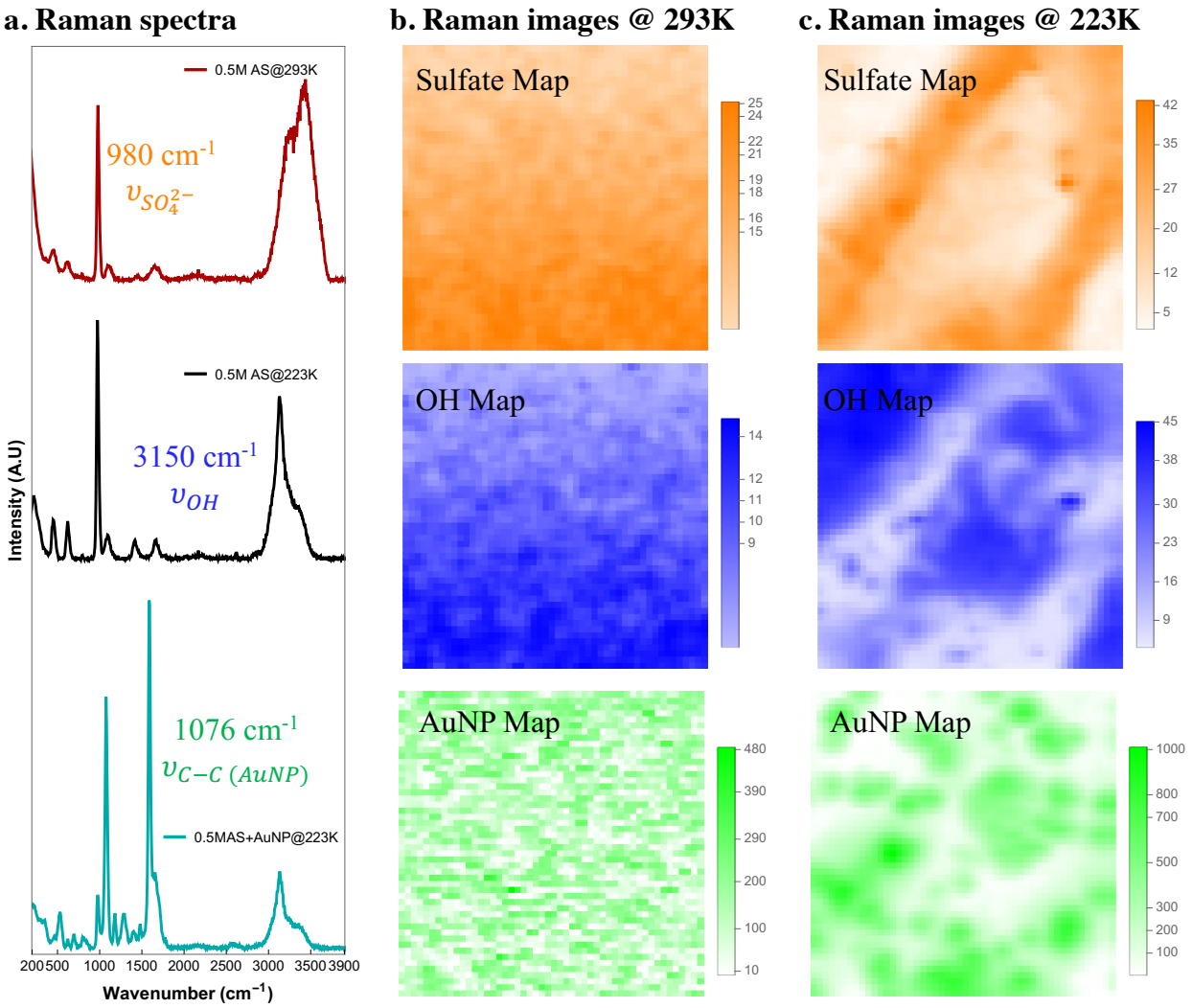

Figure 1. a) Raman spectra of 0.5M ammonium sulfate (AS) at 293K and 223K, and Raman spectrum of 0.5M AS + 4MBA functionalized AuNP at 223K. The peaks used to generate the Raman images in b) and c) are indicated. b) Raman images of sulfate (980 cm^{-1}), O-H (3230 cm^{-1}), and AuNP (1076 cm^{-1}from 4-MBA) collected at 293K. Raman images are created based upon the peak intensities indicated in panel a). Each image contains 50×50 pixels that cover a 50×50 μm^2 area. c) Raman images of sulfate (980 cm^{-1}), O-H (ice crystal, 3150 cm^{-1}), and AuNP (1076 cm^{-1}) at 223K.

Bulk ammonium sulfate solutions.

We collected Raman images of bulk AS in both liquid and frozen form at 293K and 223K to investigate the spatial variation of chemical moieties before and after freezing. The Raman signal intensity is proportional to the number density of molecules for conditions with controlled laser

intensity and integration time;[39] accordingly, a Raman image of a particular vibrational mode reflects the spatial distribution of a given ion or molecule within the imaged area.

We initially collected Raman spectra to determine how the AS spectrum changes following ice nucleation. As shown in Figure 1a, the AS solution spectrum at 293K has two major peaks: one peak at 980 cm^{-1}, corresponding to the sulfate symmetric stretch,[40,41] and another broad band at 3050-3300 cm^{-1}, which reflects the water molecule O-H vibration. The width of a Raman band, represented by the full width at half maximum (FWHM), can reflect molecular crystallinity;[42,43] therefore, the measured changes in the Raman spectrum of AS system at 223K reflect ice crystallization upon freezing. A sharp band at ≈3150 cm^{-1}, with a lower FWHM compared to the broad O-H vibration band in aqueous solution, appeared upon freezing of AS solution. This sharp band is consistent with the previously reported vibration of O-H in crystalized ice, and the shape of the band (from 3050 cm^{-1} to 3500 cm^{-1}) reflects hexagonal ice crystals that formed as aqueous water freezes.[27,44–48] Using a deuterated AS/D_2O solution, we observed a similar, but shifted, peak, further suggesting the origin of the peak is the O-H/O-D vibration (Figure S5). Importantly, the FWHM of the 980 cm^{-1} peak changed negligibly between 293K and 223K (Figure S6) and thus sulfate crystallization cannot be discriminated by monitoring the FWHM at 980 cm^{-1}. Yeung et al. observed a peak shift of the sulfate band following sulfate crystallization after efflorescence; however, no well-resolved shift of the sulfate peak location was observed in this study.

Changes in the Raman maps following freezing events in the AS/H_2O system provide additional information about crystallization. Figure 1b&1c display Raman maps of sulfate and the O-H vibration intensity at 293K and 223K respectively. These images were generated based upon the intensities of the characteristic peaks of sulfate (980 cm^{-1}) and O-H (3150 cm^{-1}) and show the distribution of sulfate and water molecule within the imaged area. Both the sulfate and O-H maps

collected at 293K show the homogeneous spatial distribution of sulfate and water in the aqueous phase. When the temperature was decreased to 223K at a rate of 10 K/min, below the apparent freezing point observed in this study(~253K), the sulfate and O-H peak intensities exhibit obvious spatial variations as reflected in the Raman maps (Figure 1c). In particular, the low temperature Raman maps exhibit spatially enriched sulfate and O-H distributions.

In some images, the sulfate and O-H enriched areas are completely complementary, while in other images, their distribution overlaps (Figure 1b&1c, Figure S7). The difference in the overlap between the sulfate and the O-H distributions indicates different freezing processes in the AS system. To quantify the difference in the overlap between the sulfate and O-H distributions, we defined the overlap ratio:

$$\text{Overlap ratio (OR)} = \frac{overlapped\ pixels\ with\ above - average\ O - H\ and\ sulfate\ signal}{pixels\ with\ above - average\ O - H\ signal}$$

OR reflects the overlapping regions of ice crystal and sulfate within a Raman image, and numerically represents the ratio of pixels with O-H and sulfate signals that are greater than the mean intensity divided by the pixels with O-H signals that are greater than the mean O-H intensity. A detailed explanation of OR can be found in the Supporting Information. Low OR suggests sulfate expulsion from the ice crystal structure. Previous studies have shown that sulfate and other salts are excluded from ice crystals due to the mismatch between the crystal structure of AS and ice. Ions in frozen electrolyte system, in the absence of supercooling, tend to enrich at the interfaces between individual ice domains.[49–51] Sulfate expulsion from ice would suggest that the majority of ammonium ions have the same spatial distribution, even though the two ions can be imbalanced within interfacial areas when ice crystals form.[51,52] The orange patterns in Figure 2a show the OR

distribution of various concentration AS bulk solutions. OR values are represented using a probability distribution since they can vary for a given AS concentration due to the stochastic nature of ice nucleation; however, in general, higher initial concentrations of AS have greater probability of higher OR values. This result is represented by the shift in the width of the probability distribution: the majority of OR values are lower than 0.5 at 0.1M&0.5M AS whereas 1M&3M AS showed a higher probability of OR values above 0.5. The enhanced probability of high OR values reflect coexisting regions of sulfate and ice. Figure 2b provides example Raman images that show virtually identical distributions of sulfate and ice crystals. The increase in AS concentration enhanced the sulfate signal intensity uniformly in the sample. The greater probability of high OR values in high AS concentration bulk systems reflects a reduction in sulfate expulsion from newly formed ice crystals following nucleation and the inhibition of AS crystallization due to the greater viscosity of higher AS concentrations.[17,49,53,54]

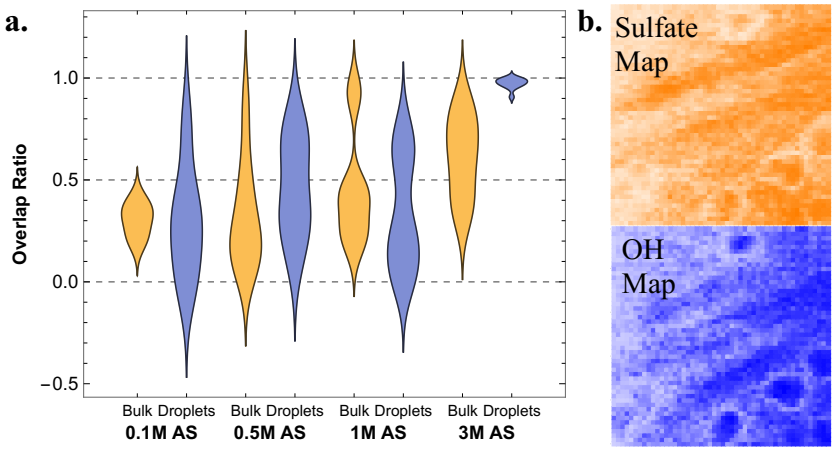

Figure 2. a) The distribution of overlap ratio (OR) calculated for Raman images of ammonium sulfate (AS) solution and droplets at 223K. The patterns denote the distribution of the OR represented by 8-10 Raman maps collected for corresponding AS bulk solutions and 10-15 Raman maps for droplets, wider parts represent higher probability of the corresponding OR. b) Raman images of 3M AS bulk system at 223K with identical distribution of sulfate and ice crystal that are denoted by high OR values.

Ammonium sulfate droplets.

The observed changes in the spatial distribution measured by Raman spectroscopy following freezing of AS demonstrate our general approach. We applied a similar imaging procedure to 10-40 μm AS droplets to investigate ice crystallization within droplets and to probe the differences between individual droplets. The findings of our previous study show that the atomization process preserves droplet composition compared to original bulk solutions and that the droplets remain stable under 293K and 95% RH.[23,38] For Raman imaging during droplet freezing, the low temperature limits the diffusion of water molecules thus leading to elongated equilibration times.[55,56] The change in the droplet size was negligible according to the optical images at 223K (Figure S3). Therefore, we assume that AS concentrations in droplets are identical to the original bulk solutions for Raman imaging at both 293K and 223K in this study. The droplets studied herein were $\approx 13 \pm 3.9\ \mu m$ on average. This average approximates the average diameter of droplet clouds and cirrus clouds of ≈10 μm.[57]. The droplet temperature was decreased at a rate of 10 K/min to minimize mass transport from supercooled droplets to ice particles due to vapor pressure differences and to suppress heterogeneous nucleation.[20] Ice particles possess a lower equilibrium vapor pressure relative to supercooled water droplets due to their greater stability. This vapor pressure difference can induce ice crystal growth.[7,58]

According to the collected optical images, about 10-80% of the AS droplets exhibited a visible change in their appearance from bright to dark at 223K. This change was dependent on the initial AS concentration (Figure 3a&3c). This temperature is comparable with literature-reported values for the freezing of AS droplets.[25,26,47,59] The occurrence of different brightness levels at 223K suggests that the droplets are in different states or phases under the same temperature condition. To characterize the difference between the bright and dark droplets, we collected Raman images of aqueous AS droplets at room temperature as well as bright and dark AS droplets at 223K. The

averaged Raman spectra from various AS droplets at 223K showed shifts in O-H peak location and variations in O-H peak shapes that indicate the different states of droplets after freezing (Figure S6). Moreover, Raman images of aqueous AS droplets at 293K consistently exhibited evenly distributed sulfate and O-H (Figure S8). In contrast, low temperature Raman maps of AS droplets showed two distinct patterns: evenly distributed or spatially enriched sulfate (Figure 3a).

To better visualize and determine the chemical moiety distribution within droplets, we transformed the Cartesian coordinates of a droplet image into distance from the droplet center (similar to polar coordinates) and Raman peak intensity to present our collected Raman images (Figure 3b). This method was used to simultaneously compare multiple collected maps and objectively differentiate evenly distributed and spatially enriched analyte distributions (Figure S9). The x-axis of the transformed graph represents the distance (d) of each pixel from the pre-defined droplet center, while the y-axis represents the relative intensity at a given distance. We used a normalized distance (d/R_0; where R_0 is the equivalent radius of a droplet) to denote the droplet edge ($d/R_0 \approx 1$) and to generate comparable length scales when overlaying transformed images because the chemical species distribution was independent of droplet size (Figure S10). In a typical droplet Raman map, pixels outside the droplet have low intensity, whereas pixels inside the droplet have higher signal intensities. We applied a threshold to set the droplet area by counting the pixels inside droplets. The as produced intensity-distance profiles succinctly categorize the homogeneity in the droplet signal intensity and its components. The signal intensity of an evenly distributed droplet, such as an aqueous AS droplet, should be flat when the normalized distance (d/R_0) is less than one and then decrease sharply near the droplet edge ($d/R_0 \approx 1$), thus resulting in a clearly defined reverse-S shape as illustrated in Figure 3b. In contrast, spatially enriched droplets have less defined patterns,

with the highest signal appearing at the most concentrated area in the droplet; however, similar to homogeneous droplets, the signal intensity decreases at the droplet edge.

Across all AS droplets, >93% of the bright droplets had evenly distributed Raman images while >90% of the dark droplets showed spatially enriched Raman images (Figure 3c). According to the observed change in the Raman image for the bulk AS system from evenly distributed at 293K to spatially enriched at 223K, which reflect ice nucleation and crystallization during the freezing, the same change in Raman images for AS droplets should also correlate with the ice nucleation and crystallization in AS droplets.

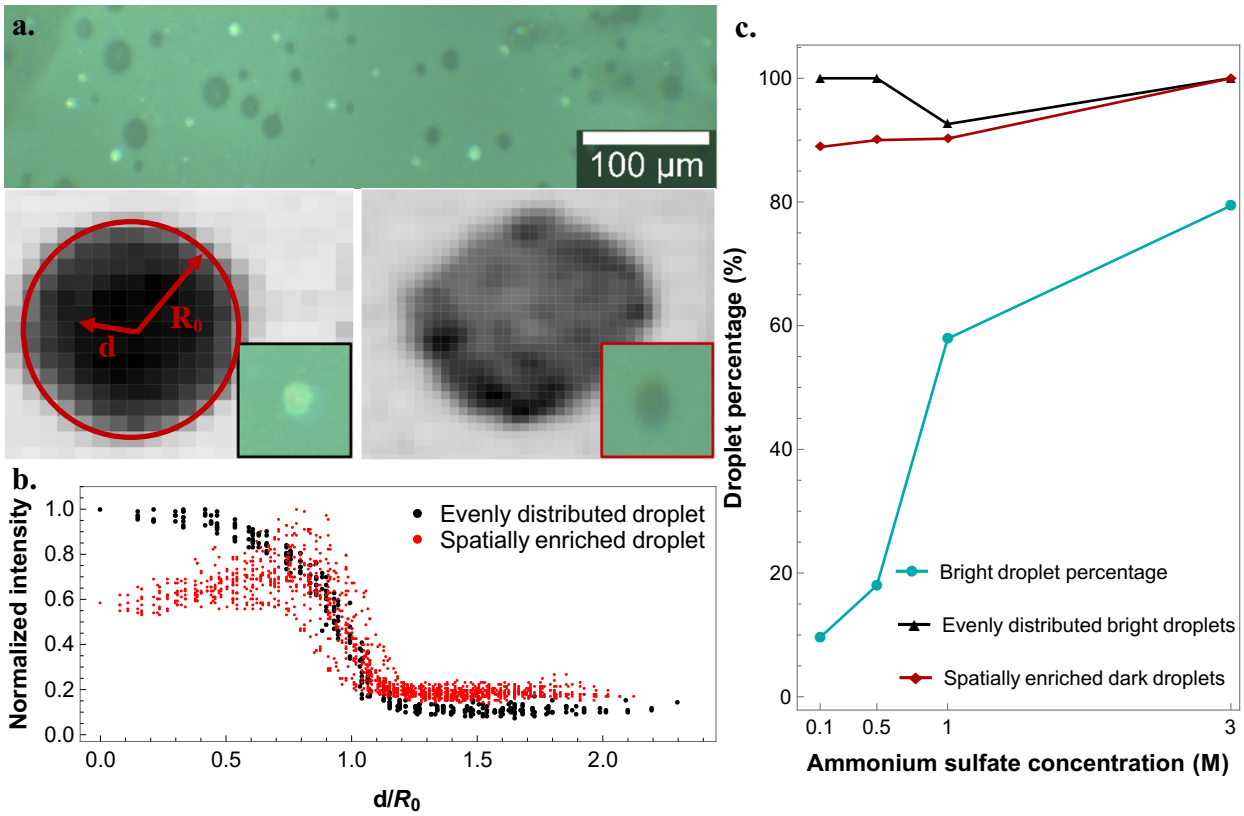

Figure 3. a) Example optical images (upper panel) and example Raman images of bright and dark droplets; b) the intensity-relative distance profile of droplets generated from the Raman images for evenly distributed droplet and spatially enriched droplet. c) The bright droplet percentage obtained from optical images (cyan line, more than 100 droplets were counted for each concentration) at 223K and the percentile of evenly distributed bright droplets (black line) and

spatially enriched dark droplets (red line) according to the intensity-relative distance profile transformed from the collected Raman images of >20 droplets for each concentration at 223K.

The droplet brightness change reflects the phase transition in the AS droplets. Our confocal Raman imaging system uses a reflected light microscope (incident light is transmitted through the objective); therefore, less absorption (more transmitted light), and greater forward-scattered or backscattered light will cause a brighter droplet image. Previous studies on ice and water droplets with similar sizes to those here (e.g., 10-40 μm), have shown that the infrared light absorption efficiency of ice droplets is >5× greater than that of water droplets.[60] The same study also showed a comparable extinction efficiency for ice and water droplets; however, the specific direction of scattered light needs to be taken into account. The side scattering of ice clouds is stronger than that of water cloud droplets in the range of 60-130°, whereas water cloud droplets exhibit greater forward (10 - 60°) and backscatter (> 160°).[61] We calculated greater backscattering of water droplets at higher angle via Mie-scattering calculations at 532 nm using previously reported refractive indices for water and ice (Figure S11).[62] The lower absorption efficiency and greater forward-scattered and backscattered light collectedly suggest that the brighter droplets observed in this study are in a supercooled aqueous state.

The strong correlation between the evenly distributed Raman images and the bright optical droplet images, as well as the correlation between the dark droplets and the spatially enriched Raman images (Figure 3c), suggest that bright evenly distributed droplets are supercooled droplets while the dark spatially enriched droplets are frozen droplets that experienced ice crystallization and the expulsion of AS upon phase transition.[17] We note that we also observed <7% of spatially enriched bright droplets, and a low percentage (<10%) of evenly distributed dark droplets. We interpret the spatially enriched bright droplets to reflect the coexistence of crystalized ice and supercooled

viscous water within a droplet, as reported previously.[29,44] The evenly distributed dark droplets suggest that a phase transition occurred within the AS droplets without crystallization. The evenly distributed Raman images reflect the amorphous solid state of these dark AS droplets. Prior studies have shown that atmospheric droplets can form glasses, an amorphous state that behaves mechanically like a solid, when droplet viscosity is high or when organic matter is present.[17,63] As the temperature decreases, the viscosity of the supercooled droplets increases and that may hinder nucleation and crystallization; therefore, we suggest the evenly distributed dark droplets are droplets that underwent glass formation.[17,64]

Following the classification of the two major droplet states at 223K, we investigated how the AS concentration affected supercooling and crystallization in droplets. We evaluated the OR of collected Raman images for both supercooled and crystallized AS droplets for AS concentrations ranging from 0.1-3 M. The distribution of AS and water molecules in supercooled droplets should be evenly distributed as observed for the aqueous phase, resulting in overlapping sulfate and O-H Raman images. Micron-size AS droplets can separate into ice crystals and freeze-concentrated AS domains below the eutectic temperature (< 254.5 K)[49] that result in compensating Raman images of O-H and sulfate. We observed a greater OR for higher AS concentrations which suggests that more droplets were supercooled under high AS concentrations.[10] Herein, we assumed homogenous ice nucleation as the dominating process for AS droplets. Because homogeneous nucleation occurs more readily when the ice saturation ($S_i = \frac{P_{H_2O}}{P_{ice}}$) is high, droplets with high AS exhibit a decrease in S_i and are more likely to be supercooled. We considered heterogenous nucleation as negligible for the following reasons. First, the estimated relative humidity (RH, equivalent to ice saturation S_i) of AS aerosols at equilibrium at 223K using the E-AIM model is 61.7%.[65] At this moderate RH, the temperature change rate we used (10K/min) should suppress mass transfer that may initiate

heterogeneous nucleation.[20] Second, the chamber environment within our thermostage contained pure air and sample droplets with no source of dust or particles that potentially serve as nuclei for heterogeneous nucleation, which can suppress the probability of heterogeneous nucleation. Third, our substrate is superhydrophobic which minimizes the effect of the surface on heterogeneous nucleation.[48] Surface roughness can promote heterogeneous nucleation;[66,67] therefore, we further sought to evaluate the probability of surface-induced heterogeneous nucleation by testing two other hydrophobic filters (PTFE filter and silane-coated aluminum). We observed similar phenomenon for the three substrates (Figure S12).

The bright droplet percentage denoted by the cyan line (indicated by circles) in Figure 3c shows an increasing percentage of bright droplets with an increase in the AS concentration that reflects the higher probability of droplet supercooling at high AS concentration as the bright droplet percentage is strongly corelated with the percentage of supercooled droplets. This result agrees with the droplet results in OR in Figure 2a. This bright droplet percentage is equivalent to the frozen fraction commonly defined in ice nucleation studies.[50,68] We also determined the bright droplet percentage ($\frac{\text{Number of bright droplets}}{\text{Number of total droplets}} \times 100\%$) of 1M ammonium nitrate (AN) and 1M phosphate buffer (PB, solution pH =7.4) droplets (Figure S13). The droplet number percentage of 1M AN was comparable to 1M AS. AS and AN solution have similar viscosity[53,69], and E-AIM calculation gave similar equilibrium RH value (<1% difference) for AS and AN droplets which denote similar water activity in droplets. Given that homogeneous nucleation dominates in this study, we expect ice nucleation activity in AS and AN droplets to be similar, since the process is primarily dictated by water activity and is affected by viscosity.[17,70] The phosphate droplets exhibited a significantly higher ratio of bright droplets at the same temperature thus implying a higher probability of droplet supercooling and lower ice nucleation activity in PB droplets. This

difference between PB droplets and ammonium droplets suggests the effect arises from viscosity differences,[71,72], and different ice nucleation processes in the multicomponent PB.

The ratio of bright droplets and dark droplets can be correlated with the Boltzmann distribution. According to the Boltzmann distribution, this ratio can be expressed in terms of energy:

$$\frac{N_{state1}}{N_{state2}} = e^{-\frac{\Delta\epsilon}{kT}}$$

where $\Delta\epsilon$ is the thermodynamic energy difference between two states (e.g., supercooled droplet vs. crystalized droplets, or crystallite vs. glass formation). We estimated the apparent $\Delta\epsilon$ between supercooling and crystallization for 0.1, 0.5, 1, and 3M AS to be ~2.2 kT, 1.5 kT, -0.3 kT, and -1.3 kT respectively. These values refer to the difference in thermodynamic free energy. The droplet number percentage of AS, AN, and PB droplets changed only after the system reached 223K (Figure S13). Similarly, the change in the brightness of the AS droplets occurred after the system reached a certain temperature (223K, Figure S3). These two phenomena reflect that kinetic activation is required to initiate nucleation and cyrstalization.[12] The values achieved from the Boltzmann distribution were about 10× lower than the kinetic activation energy for bulk homogeneous ice nucleation reported previously.[12] Since freezing is a kinetically controlled nucleation process, and previous studies have shown that larger droplets tend to crystallize at a higher rate[54], the smaller thermodynamic energy can be attributed to: 1) the dominant kinetic parameters during ice nucleation; 2) the lower energy requirements for micron-size droplet freezing compared to bulk solution. We note that the Boltzmann analysis provides only a qualitative assessment of the energy given the finite number of droplets. Moreover, we categorize the evenly distributed dark droplets as those that experienced glass formation; accordingly, with

additional droplet data that correlates with both evenly distributed and spatially enriched dark droplets, we will be able to estimate the free energy difference between glass formation and crystallization via droplet counting and the Boltzmann analysis.

Gold nanoparticle in ammonium sulfate system.

Using Raman imaging, we have shown that the distribution of sulfate and ice in droplets upon freezing varies between individual droplets for AS concentrations < 3M. In parallel, we observed the distribution of the 4-mercaptobenzoic acid (4-MBA) functionalized AuNPs (pH nanoprobe) within the frozen AS system. This study was conducted to investigate the correlation between the distribution of the pH nanoprobe and the ice crystal growth. Raman images of the pH nanoprobe were collected according to its peak intensity at 1076 cm^{-1} which originates from the 4-MBA benzene breathing mode.[23,37] Similar to the AS solution, the pH nanoprobes were evenly distributed at room temperature, but spatially enriched after being frozen in both bulk and droplets which reflects the previously reported nanoparticle embedded in ice (Figure 1, Figure S7).[73–75] We also conducted multiple freeze-thaw cycles on the pH nanoprobe suspension, and demonstrated the stabilization effect of polymer coating on the pH nanoprobe (Figure 4a). The collected images show the independent distribution of AuNPs relative to the distribution of either AS or ice crystal under the conditions of this study (Figure 1c&S7, AuNPs are enriched within both AS rich domains and ice crystal domains). The aggregation of AuNPs without polymer coating should have identical distribution with salt due to the exclusion by the growing ice crystal.[75] The independent distribution of the pH nanoprobes observed in this study can be attributed to the colloidal stabilization effect of the PEG polymer coating and the hydroxyl end group of PEG. We observed no apparent change in the droplet number ratio of the droplets that contained AuNPs (~22% in 1M AS droplets), which suggests negligible immersion freezing and little effect on the

kinetics of ice nucleation in the presence of relatively low concentrations of pH nanoprobes (~10^9 NPs/L).

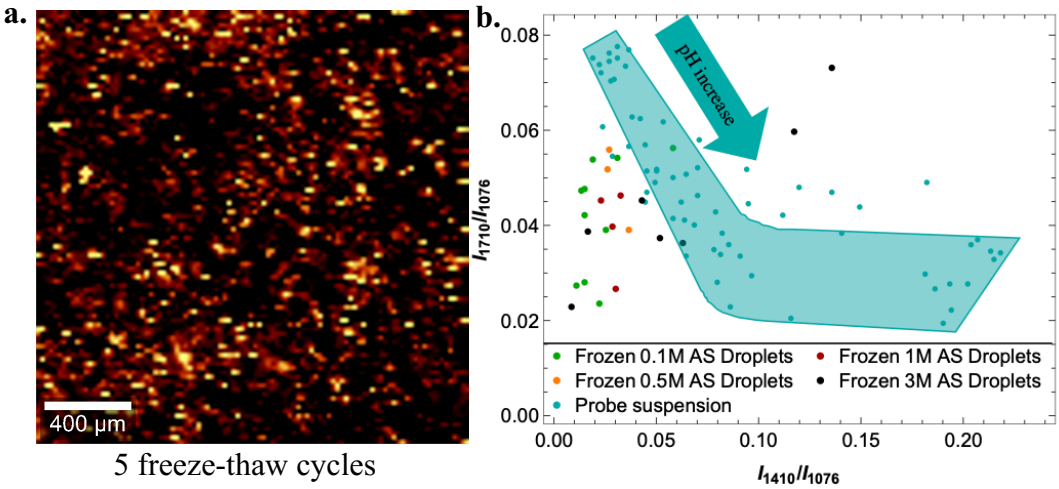

Figure 4. a) The distribution of pH nanoprobe in the pH nanoprobe suspension after 5 freeze-thaw cycles. b) The correlation between two peak ratios I_{1710}/I_{1076} and I_{1410}/I_{1076} at different solution pH (from 2-12). The cyan region denotes the peak ratios of pH nanoprobe in suspensions of different pH at 293K. Both peak ratios can be applied to quantify the suspension pH in aqueous phase. The correlation of two peak ratios under 223K completely deviated from that observed in aqueous suspension (cyan region).

In our previous studies, we applied 4-MBA functionalized AuNPs with SERS imaging to achieve pH quantification and imaging of micron-size droplets.[23,38] The weak correlation between aggregated AuNP and ice crystals in the AS system provided us with the potential to characterize pH in different domains within the AS system, and to investigate the pH difference between supercooled and crystalized droplets. Investigating pH changes that occur following droplet freezing may provide important information on ion enrichment and potentially the imbalance of ions caused by ice crystallization.[51] We evaluated the spectral behavior of the spatially enriched pH nanoprobes. In aqueous solutions, the Raman spectrum of the pH nanoprobe correlates well with the surrounding pH due to the protonation and deprotonation of the carboxyl group of 4-MBA. At low pH conditions, the higher abundance of protonated 4-MBA results in higher intensity of 1710 cm^{-1} peak (I_{1710}) and reduced intensity of the 1410 cm^{-1} peak (I_{1410}). To minimize signal

385 variability the pH sensitive peaks are normalized to the pH intensity peak at 1076 cm^{-1} (I_{1076}) which
386 is originated from benzene ring-breathing mode.[23,37,38] pH nanoprobe suspensions with different
387 pH values (4 - 11) were prepared using 1M HCl and 1M NaOH after synthesis, and characterized
388 by Raman spectroscopy after pH adjustment. The correlation between the two peak ratios (I_{1410}/I_{1076}
389 and I_{1710}/I_{1076}) in aqueous solutions are depicted by the cyan region in Figure 4b. At 223K, the
390 correlation between the two peak ratios of the pH nanoprobe upon freezing (represented by dots
391 in non-cyan colors) deviated from that obtained in the aqueous phase. Moreover, the peak ratios
392 changed greatly within droplets with the same AS concentration (Figure 4b). The large variance
393 in spectral behavior suggests that the aggregation of AuNPs alters the Raman spectra at 223K. A
394 previous study has shown that changes in the orientation and binding modes of a molecule on the
395 gold nanoparticle surface can alter its spectrum.[76] Therefore, the spectral changes we observed can
396 be attributed to the change in molecular orientation in the aggregation of AuNPs and the change
397 in protonation of the carboxylic group of the pH nanoprobe in the ice crystals at 223K. The spectral
398 changes also indicate a state different from the aqueous state at 293K, which can be related to the
399 aggregation and assembly of pH nanoprobes at 223K. To achieve pH characterization in different
400 domains of ice, future study is needed to figure out how the functional group (4-MBA) was
401 affected by the assembly and aggregation of pH nanoprobes during ice crystal growth.

402 **Conclusions**

403 In this study we demonstrate that low temperature (223K) Raman and SERS imaging are reliable
404 tools to investigate molecule and ion distribution which can provide micro-meter scale resolution.
405 Using low temperature Raman imaging, we observed the exclusion of sulfate from ice crystal
406 during the freezing of AS solution. Both AS bulk system and AS droplets exhibited various
407 freezing processes indicated by the OR value evaluated from Raman images. The droplets at 223K

showed different states that reflects the stochastic nature of ice nucleation. The population of droplets in different states that are characterized by Raman imaging can provide qualitative estimation of the thermodynamic energy difference between the states. We studied the distribution of pH nanoprobes separately using SERS imaging, which has the same experimental setup with Raman imaging. The distribution of pH nanoprobe are independent from either icy crystal or sulfate distribution, which provide the potential for the pH nanoprobe on charactering pH in different ice domains. However, the freezing processes altered the spectral behavior of pH nanoprobe; therefore, future studies on factors affect pH nanoprobe SERS spectra is required. Our findings in this study show the potential of low-temperature Raman and SERS imaging on micron-level characterization that can provide fundamental physical chemistry insights.

AUTHOR INFORMATION

Corresponding Author

*Qishen Huang – Virginia Tech, Blacksburg, Virginia, 24060, United States; The author is currently at The Pennsylvania State University, University Park, Pennsylvania, 16802, United States; Email: qqh5081@psu.edu; Phone: (434)-326-8290

Funding Sources

This research was supported by the National Science Foundation (CBET-1705653).

ASSOCIATED CONTENT

Supporting Information. Additional information on experimental details and supportive graphs involved in the discussion and method section are included in the supporting information.

ACKNOWLEDGMENT

We would like to thank Dr. Weinan Leng for his assistance in Linkam thermostage operation and Raman experiments, and the Virginia Tech Institute of Technology and Applied Science (ICTAS) and center for Sustainable Nanotechnology for providing the instruments.

References

(1) Signorell, R.; Bertram, A.; Knopf, D. A.; Lopez, M. D. Homogeneous Ice Freezing Temperatures and Ice Nucleation Rates of Aqueous Ammonium Sulfate and Aqueous Levoglucosan Particles for Relevant Atmospheric Conditions. *Phys. Chem. Chem. Phys.* **2009**, *11* (36), 7759. https://doi.org/10.1039/b916865f.

(2) Rosenfeld, D. Suppression of Rain and Snow by Urban and Industrial Air Pollution. *Science (80-.).* **2000**, *287* (5459), 1793–1796. https://doi.org/10.1126/science.287.5459.1793.

(3) Baker, M. B.; Peter, T. Small-Scale Cloud Processes and Climate. *Nature* **2008**, *451* (7176), 299–300. https://doi.org/10.1038/nature06594.

(4) Krämer, M.; Schiller, C.; Voigt, C.; Schlager, H.; Popp, P. J. A Climatological View of HNO3 Partitionong in Cirrus Clouds. *Q. J. R. Meteorol. Soc.* **2008**, *134* (633 B), 905–912. https://doi.org/10.1002/qj.253.

(5) Jensen, E.; Pfister, L. Implications of Persistent Ice Supersaturation in Cold Cirrus for Stratospheric Water Vapor. *Geophys. Res. Lett.* **2005**, *32* (1), 1–4. https://doi.org/10.1029/2004GL021125.

(6) Pruppacher, H. R.; Klett, J. D. *Microphysics of Clouds and Precipitation*, 2nd ed.;

Atmospheric and Oceanographic Sciences Library; Springer Netherlands: Dordrecht, 2010; Vol. 18. https://doi.org/10.1007/978-0-306-48100-0.

(7) Murray, B. J.; O'sullivan, D.; Atkinson, J. D.; Webb, M. E. Ice Nucleation by Particles Immersed in Supercooled Cloud Droplets. *Chem. Soc. Rev.* **2012**, *41* (19), 6519–6554. https://doi.org/10.1039/c2cs35200a.

(8) Tabazadeh, A.; Djikaev, Y. S.; Reiss, H. *Surface Crystallization of Supercooled Water in Clouds*; 2002; Vol. 99. https://doi.org/10.1073/pnas.252640699.

(9) Rosenfeld, D.; Woodley, W. L. Deep Convective Clouds with Sustained Supercooled Liquid Water down to - 37.5 °C. *Nature* **2000**, *405* (6785), 440–442. https://doi.org/10.1038/35013030.

(10) Bertram, A. K.; Koop, T.; Molina, L. T.; Molina, M. J. Ice Formation in (NH4)2so4-H2O Particles. *J. Phys. Chem. A* **2000**, *104* (3), 584–588. https://doi.org/10.1021/jp9931197.

(11) Espinosa, J. R.; Vega, C.; Sanz, E. Homogeneous Ice Nucleation Rate in Water Droplets. *J. Phys. Chem. C* **2018**, *122* (40), 22892–22896. https://doi.org/10.1021/acs.jpcc.8b04788.

(12) Ickes, L.; Welti, A.; Hoose, C.; Lohmanna, U. Classical Nucleation Theory of Homogeneous Freezing of Water: Thermodynamic and Kinetic Parameters. *Phys. Chem. Chem. Phys.* **2015**, *17* (8), 5514–5537. https://doi.org/10.1039/c4cp04184d.

(13) Koop, T.; Luo, B.; Tsias, A.; Peter, T. *Water Activity as the Determinant for Homogeneous Ice Nucleation in Aqueous Solutions*; 2000; Vol. 406. https://doi.org/10.1038/35020537.

(14) Ault, A. P.; Axson, J. L. Atmospheric Aerosol Chemistry: Spectroscopic and Microscopic Advances. *Anal. Chem.* **2017**, *89* (1), 430–452. https://doi.org/10.1021/acs.analchem.6b04670.

(15) Martin, S. T. Phase Transitions of Aqueous Atmospheric Particles. *Chem. Rev.* **2000**, *100* (9), 3403–3453. https://doi.org/10.1021/cr990034t.

(16) Marcolli, C.; Luo, B.; Peter, T. Mixing of the Organic Aerosol Fractions: Liquids as the Thermodynamically Stable Phases. *J. Phys. Chem. A* **2004**, *108* (12), 2216–2224. https://doi.org/10.1021/jp036080l.

(17) Zobrist, B.; Marcolli, C.; Pedernera, D. A.; Koop, T. *Do Atmospheric Aerosols Form Glasses?*; 2008; Vol. 8. https://doi.org/10.5194/acp-8-5221-2008.

(18) Schlenker, J. C.; Martin, S. T. Crystallization Pathways of Sulfate-Nitrate-Ammonium Aerosol Particles. *J. Phys. Chem. A* **2005**, *109* (44), 9980–9985. https://doi.org/10.1021/jp052973x.

(19) Freedman, M. A. Phase Separation in Organic Aerosol. *Chem. Soc. Rev.* **2017**, *46* (24), 7694–7705. https://doi.org/10.1039/c6cs00783j.

(20) Koop, T.; Ng, H. P.; Molina, L. T.; Molina, M. J. A New Optical Technique to Study Aerosol Phase Transitions: The Nucleation of Ice from H2SO4 Aerosols. *J. Phys. Chem. A* **1998**, *102* (45), 8924–8931. https://doi.org/10.1021/jp9828078.

(21) Chelf, J. H.; Martin, S. T. Homogeneous Ice Nucleation in Aqueous Ammonium Sulfate Aerosol Particles. *J. Geophys. Res. Atmos.* **2001**, *106* (1), 1215–1226.

https://doi.org/10.1029/2000jd900477.

(22) Rigg, Y. J.; Alpert, P. A.; Knopf, D. A. Immersion Freezing of Water and Aqueous Ammonium Sulfate Droplets Initiated by Humic-like Substances as a Function of Water Activity. *Atmos. Chem. Phys.* **2013**, *13* (13), 6603–6622. https://doi.org/10.5194/acp-13-6603-2013.

(23) Huang, Q.; Wei, H.; Marr, L. C.; Vikesland, P. J. Direct Quantification of the Effect of Ammonium on Aerosol Droplet PH. *Environ. Sci. Technol.* **2021**, *55* (1), 778–787. https://doi.org/10.1021/acs.est.0c07394.

(24) Pye, H.; Nenes, A.; Alexander, B.; Ault, A.; Barth, M.; Clegg, S.; Collett Jr., J.; Fahey, K.; Hennigan, C.; Herrmann, H.; Kanakidou, M.; Kelly, J.; Ku, I.-T.; McNeill, V. F.; Riemer, N.; Schaefer, T.; Shi, G.; Tilgner, A.; Walker, J.; Wang, T.; Weber, R.; Xing, J.; Zaveri, R.; Zuend, A. *The Acidity of Atmospheric Particles and Clouds*; 2019. https://doi.org/10.5194/acp-2019-889.

(25) Cziczo, D. J.; Abbatt, J. P. D. Deliquescence, Efflorescence, and Supercooling of Ammonium Sulfate Aerosols at Low Temperature: Implications for Cirrus Cloud Formation and Aerosol Phase in the Atmosphere. *J. Geophys. Res. Atmos.* **1999**, *104* (D11), 13781–13790. https://doi.org/10.1029/1999JD900112.

(26) Hung, H. M.; Malinowski, A.; Martin, S. T. Ice Nucleation Kinetics of Aerosols Containing Aqueous and Solid Ammonium Sulfate Particles. *J. Phys. Chem. A* **2002**, *106* (2), 293–306. https://doi.org/10.1021/jp012064h.

(27) Celli, M.; Ulivi, L.; Del Rosso, L. Raman Investigation of the Ice Ic-Ice Ih

Transformation. *J. Phys. Chem. C* **2020**, *124* (31), 17135–17140. https://doi.org/10.1021/acs.jpcc.0c05136.

(28) Ben Mabrouk, K.; Kauffmann, T. H.; Aroui, H.; Fontana, M. D. Raman Study of Cation Effect on Sulfate Vibration Modes in Solid State and in Aqueous Solutions. *J. Raman Spectrosc.* **2013**, *44* (11), 1603–1608. https://doi.org/10.1002/jrs.4374.

(29) Jenniskens, P.; Banham, S. F.; Blake, D. F.; McCoustra, M. R. S. Liquid Water in the Domain of Cubic Crystalline Ice Ic. *J. Chem. Phys.* **1997**, *107* (4), 1232–1241. https://doi.org/10.1063/1.474468.

(30) Riemer, N.; Ault, A. P.; West, M.; Craig, R. L.; Curtis, J. H. Aerosol Mixing State: Measurements, Modeling, and Impacts. *Rev. Geophys.* **2019**, *57* (2), 187–249. https://doi.org/10.1029/2018RG000615.

(31) Yeung, M. C.; Chan, C. K. Water Content and Phase Transitions in Particles of Inorganic and Organic Species and Their Mixtures Using Micro-Raman Spectroscopy. *Aerosol Sci. Technol.* **2010**, *44* (4), 269–280. https://doi.org/10.1080/02786820903583786.

(32) Mael, L. E.; Busse, H.; Grassian, V. H. Measurements of Immersion Freezing and Heterogeneous Chemistry of Atmospherically Relevant Single Particles with Micro-Raman Spectroscopy. *Anal. Chem.* **2019**, *91* (17), 11138–11145. https://doi.org/10.1021/acs.analchem.9b01819.

(33) Guo, X.; Xiao, H. S.; Wang, F.; Zhang, Y. H. Micro-Raman and FTIR Spectroscopic Observation on the Phase Transitions of MnSO4 Droplets and Ionic Interactions between Mn2+ and SO42-. *J. Phys. Chem. A* **2010**, *114* (23), 6480–6486.

https://doi.org/10.1021/jp9104147.

(34) Craig, R. L.; Bondy, A. L.; Ault, A. P. Computer-Controlled Raman Microspectroscopy (CC-Raman): A Method for the Rapid Characterization of Individual Atmospheric Aerosol Particles. *Aerosol Sci. Technol.* **2017**, *51* (9), 1099–1112. https://doi.org/10.1080/02786826.2017.1337268.

(35) Collier, K. N.; Brooks, S. D. Role of Organic Hydrocarbons in Atmospheric Ice Formation via Contact Freezing. *J. Phys. Chem. A* **2016**, *120* (51), 10169–10180. https://doi.org/10.1021/acs.jpca.6b11890.

(36) Schill, G. P.; Tolbert, M. A. Heterogeneous Ice Nucleation on Simulated Sea-Spray Aerosol Using Raman Microscopy. *J. Phys. Chem. C* **2014**, *118* (50), 29234–29241. https://doi.org/10.1021/jp505379j.

(37) Wei, H.; Willner, M. R.; Marr, L. C.; Vikesland, P. J. Highly Stable SERS PH Nanoprobes Produced by Co-Solvent Controlled AuNP Aggregation. *Analyst* **2016**, *141* (17), 5159–5169. https://doi.org/10.1039/c6an00650g.

(38) Wei, H.; Vejerano, E. P.; Leng, W.; Huang, Q.; Willner, M. R.; Marr, L. C.; Vikesland, P. J. Aerosol Microdroplets Exhibit a Stable PH Gradient. *Proc. Natl. Acad. Sci.* **2018**, *115* (28), 7272–7277. https://doi.org/10.1073/pnas.1720488115.

(39) Peter Larkin. *Infrared and Raman Spectroscopy, 2nd Edition*, 2nd ed.; Elsevier, 2017.

(40) Venkateswarlu, P.; Bist, H. D.; Jain, Y. S. Laser Excited Raman Spectrum of Ammonium Sulfate Single Crystal. *J. Raman Spectrosc.* **1975**, *3* (2–3), 143–151.

https://doi.org/10.1002/jrs.1250030205.

(41) Zhang, Y. H.; Chan, C. K. Understanding the Hygroscopic Properties of Supersaturated Droplets of Metal and Ammonium Sulfate Solutions Using Raman Spectroscopy. *J. Phys. Chem. A* **2002**, *106* (2), 285–292. https://doi.org/10.1021/jp012694j.

(42) Agarwal, U. P.; Ralph, S. A.; Reiner, R. S.; Baez, C. Probing Crystallinity of Never-Dried Wood Cellulose with Raman Spectroscopy. *Cellulose* **2016**, *23* (1), 125–144. https://doi.org/10.1007/s10570-015-0788-7.

(43) Graf, D.; Molitor, F.; Ensslin, K.; Stampfer, C.; Jungen, A.; Hierold, C.; Wirtz, L. Raman Imaging of Graphene. *Solid State Commun.* **2007**, *143* (1–2), 44–46. https://doi.org/10.1016/j.ssc.2007.01.050.

(44) Mallamace, F.; Broccio, M.; Corsaro, C.; Faraone, A.; Majolino, D.; Venuti, V.; Liu, L.; Mou, C. Y.; Chen, S. H. *Evidence of the Existence of the Low-Density Liquid Phase in Supercooled, Confined Water*; 2007; Vol. 104. https://doi.org/10.1073/pnas.0607138104.

(45) Sun, Q.; Zheng, H. Raman OH Stretching Vibration of Ice Ih. *Prog. Nat. Sci.* **2009**, *19* (11), 1651–1654. https://doi.org/10.1016/j.pnsc.2009.06.010.

(46) Sbroscia, M.; Sodo, A.; Bruni, F.; Corridoni, T.; Ricci, M. A. OH Stretching Dynamics in Hydroxide Aqueous Solutions. *J. Phys. Chem. B* **2018**, *122* (14), 4077–4082. https://doi.org/10.1021/acs.jpcb.8b01094.

(47) Ishizaka, S.; Wada, T.; Kitamura, N. In Situ Observations of Freezing Processes of Single Micrometer-Sized Aqueous Ammonium Sulfate Droplets in Air. *Chem. Phys. Lett.* **2011**,

506 (1–3), 117–121. https://doi.org/10.1016/j.cplett.2011.02.058.

(48) Koop, T.; Ng, H. P.; Molina, L. T.; Molina, M. J. A New Optical Technique to Study Aerosol Phase Transitions: The Nucleation of Ice from H2SO4 Aerosols. *J. Phys. Chem. A* **1998**, *102* (45), 8924–8931. https://doi.org/10.1021/jp9828078.

(49) Bogdan, A. Double Freezing of (NH4)2SO4/H 2O Droplets below the Eutectic Point and the Crystallization of (NH4)2SO4 to the Ferroelectric Phase. *J. Phys. Chem. A* **2010**, *114* (37), 10135–10139. https://doi.org/10.1021/jp105699s.

(50) Chong, E.; King, M.; Marak, K. E.; Freedman, M. A. The Effect of Crystallinity and Crystal Structure on the Immersion Freezing of Alumina. *J. Phys. Chem. A* **2019**, *123* (12), 2447–2456. https://doi.org/10.1021/acs.jpca.8b12258.

(51) Watanabe, H.; Otsuka, T.; Harada, M.; Okada, T. Imbalance between Anion and Cation Distribution at Ice Interface with Liquid Phase in Frozen Electrolyte as Evaluated by Fluorometric Measurements of PH. *J. Phys. Chem. C* **2014**, *118* (29), 15723–15731. https://doi.org/10.1021/jp5031653.

(52) Gerardo Wolfgang, G. Ion Distribution and Phase Boundary Potentials during the Freezing of Very Dilute Ionic Solutions at Uniform Rates. *J. Colloid Interface Sci.* **1967**, *25* (2), 270–279. https://doi.org/10.1016/0021-9797(67)90030-6.

(53) Nikam, P. S.; Aber, J. S.; Kharat, S. J. Viscosities of Ammonium Sulfate, Potassium Sulfate, and Aluminum Sulfate in Water and Water + N,N-Dimethylformamide Mixtures at Different Temperatures. *J. Chem. Eng. Data* **2008**, *53* (10), 2469–2472. https://doi.org/10.1021/je800330d.

(54) Murray, B. J.; Bertram, A. K. Inhibition of Solute Crystallisation in Aqueous H+-NH 4+-SO42--H2O Droplets. *Phys. Chem. Chem. Phys.* **2008**, *10* (22), 3287–3301. https://doi.org/10.1039/b802216j.

(55) Lu, J. W.; Rickards, A. M. J.; Walker, J. S.; Knox, K. J.; Miles, R. E. H.; Reid, J. P.; Signorell, R. Timescales of Water Transport in Viscous Aerosol: Measurements on Sub-Micron Particles and Dependence on Conditioning History. *Phys. Chem. Chem. Phys.* **2014**, *16* (21), 9819–9830. https://doi.org/10.1039/c3cp54233e.

(56) O'Meara, S.; Topping, D. O.; McFiggans, G. The Rate of Equilibration of Viscous Aerosol Particles. *Atmos. Chem. Phys.* **2016**, *16* (8), 5299–5313. https://doi.org/10.5194/acp-16-5299-2016.

(57) Sassen, K.; Zhao, H. Lidar Multiple Scattering in Water Droplet Clouds: Toward an Improved Treatment. *Opt. Rev.* **1995**, *2* (5), 394–400. https://doi.org/10.1007/s10043-995-0394-2.

(58) Murphy, D. M.; Koop, T. Review of the Vapour Pressures of Ice and Supercooled Water for Atmospheric Applications. *Q. J. R. Meteorol. Soc.* **2005**, *131* (608), 1539–1565. https://doi.org/10.1256/qj.04.94.

(59) Larson, B. H.; Swanson, B. D. Experimental Investigation of the Homogeneous Freezing of Aqueous Ammonium Sulfate Droplets. *J. Phys. Chem. A* **2006**, *110* (5), 1907–1916. https://doi.org/10.1021/jp054270l.

(60) Mitchell, D. L. Parameterization of the Mie Extinction and Absorption Coefficients for Water Clouds. *J. Atmos. Sci.* **2000**, *57* (9), 1311–1326. https://doi.org/10.1175/1520-

0469(2000)057<1311:POTMEA>2.0.CO;2.

(61) Sassen, K.; Liou, K.-N. Scattering of Polarized Laser Light by Water Droplet, Mixed-Phase and Ice Crystal Clouds. Part II: Angular Depolarizing and Multiple-Scattering Behavior. *J. Atmos. Sci.* **1979**, *36* (5), 852–861. https://doi.org/10.1175/1520-0469(1979)036<0852:sopllb>2.0.co;2.

(62) Adriani, A.; Deshler, T.; Di Donfrancesco, G.; Gobbi, G. P. Polar Stratospheric Clouds and Volcanic Aerosol during Spring 1992 over McMurdo Station, Antarctica: Lidar and Particle Counter Comparisons. *J. Geophys. Res.* **1995**, *100* (D12). https://doi.org/10.1029/95jd02029.

(63) Debenedetti, P. G.; Stillinger, F. H. *Supercooled Liquids and the Glass Transition*; 2001; Vol. 410. https://doi.org/10.1038/35065704.

(64) Kissinger, J. A.; Buttke, L. G.; Vinokur, A. I.; Guzei, I. A.; Beyer, K. D. Solubilities and Glass Formation in Aqueous Solutions of the Sodium Salts of Malonic Acid with and Without Ammonium Sulfate. *J. Phys. Chem. A* **2016**, *120* (21), 3827–3834. https://doi.org/10.1021/acs.jpca.6b02656.

(65) Wexler, A. S.; Clegg, S. L. Atmospheric Aerosol Models for Systems Including the Ions H+, NH4+, Na+, So42-, NO 3-, Cl-, Br-, and H2O. *J. Geophys. Res. Atmos.* **2002**, *107* (14). https://doi.org/10.1029/2001JD000451.

(66) Campbell, J. M.; Meldrum, F. C.; Christenson, H. K. Is Ice Nucleation from Supercooled Water Insensitive to Surface Roughness? *J. Phys. Chem. C* **2015**, *119* (2), 1164–1169. https://doi.org/10.1021/jp5113729.

(67) Bi, Y.; Cao, B.; Li, T. Enhanced Heterogeneous Ice Nucleation by Special Surface Geometry. *Nat. Commun.* **2017**, *8*. https://doi.org/10.1038/ncomms15372.

(68) Vali, G.; DeMott, P. J.; Möhler, O.; Whale, T. F. Technical Note: A Proposal for Ice Nucleation Terminology. *Atmos. Chem. Phys.* **2015**, *15* (18), 10263–10270. https://doi.org/10.5194/acp-15-10263-2015.

(69) Wahab, A.; Mahiuddin, S. Electrical Conductivity, Speeds of Sound, and Viscosity of Aqueous Ammonium Nitrate Solutions. *Can. J. Chem.* **2001**, *79* (8), 1207–1212. https://doi.org/10.1139/cjc-79-8-1207.

(70) Koop, T.; Luo, B.; Tsias, A.; Peter, T. Water Activity as the Determinant for Homogeneous Ice Nucleation in Aqueous Solutions. *Nature* **2000**, *406* (6796), 611–614. https://doi.org/10.1038/35020537.

(71) Sadeghi, R.; Jamehbozorg, B. Volumetric and Viscosity Studies of Interactions between Sodium Phosphate Salts and Poly(Propylene Glycol) 400 in Aqueous Solutions at Different Temperatures. *Fluid Phase Equilib.* **2009**, *284* (2), 86–98. https://doi.org/10.1016/j.fluid.2009.06.016.

(72) Nikam, P. S.; Aber, J. S.; Kharat, S. J. Viscosities of Ammonium Sulfate, Potassium Sulfate, and Aluminum Sulfate in Water and Water + N,N-Dimethylformamide Mixtures at Different Temperatures. *J. Chem. Eng. Data* **2008**, *53* (10), 2469–2472. https://doi.org/10.1021/je800330d.

(73) Deville, S. *Freezing Colloids: Observations, Principles, Control, and Use*; Engineering Materials and Processes; Springer International Publishing: Cham, 2017.

https://doi.org/10.1007/978-3-319-50515-2.

(74) Richardson, H. H.; Hickman, Z. N.; Govorov, A. O.; Thomas, A. C.; Zhang, W.; Kordesch, M. E. Thermooptical Properties of Gold Nanoparticles Embedded in Ice: Characterization of Heat Generation and Melting. *Nano Lett*. **2006**, *6* (4), 783–788. https://doi.org/10.1021/nl060105l.

(75) Liu, B.; Liu, J. Freezing Directed Construction of Bio/Nano Interfaces: Reagentless Conjugation, Denser Spherical Nucleic Acids, and Better Nanoflares. *J. Am. Chem. Soc*. **2017**, *139* (28), 9471–9474. https://doi.org/10.1021/jacs.7b04885.

(76) Al-Johani, H.; Abou-Hamad, E.; Jedidi, A.; Widdifield, C. M.; Viger-Gravel, J.; Sangaru, S. S.; Gajan, D.; Anjum, D. H.; Ould-Chikh, S.; Hedhili, M. N.; Gurinov, A.; Kelly, M. J.; Eter, M. El; Cavallo, L.; Emsley, L.; Basset, J. M. The Structure and Binding Mode of Citrate in the Stabilization of Gold Nanoparticles. *Nat. Chem*. **2017**, *9* (9), 890–895. https://doi.org/10.1038/nchem.2752.